2004

Effect of Porosity on the Capacity Fade of a Lithium-Ion Battery: Theory

Godfrey Sikha
University of South Carolina - Columbia

Branko N. Popov
University of South Carolina - Columbia, popov@engr.sc.edu

Ralph E. White
University of South Carolina - Columbia, white@cec.sc.edu

Follow this and additional works at: https://scholarcommons.sc.edu/eche_facpub

Part of the Chemical Engineering Commons

Publication Info

Effect of Porosity on the Capacity Fade of a Lithium-Ion Battery

Theory

Godfrey Sikha,* **Branko N. Popov,**** and **Ralph E. White***,z

Department of Chemical Engineering, University of South Carolina, Columbia, South Carolina 29208, USA

A mathematical model is presented to predict the performance of a lithium-ion battery. It includes the changes in the porosity of the material due to the reversible intercalation processes and the irreversible parasitic reaction. The model was also extended to predict the capacity fade in a lithium-ion battery based on the unwanted parasitic reaction that consumes Li^+ along with the changes in the porosities of the electrodes with cycling due to the continuous parasitic side reaction. The model can be used to predict the drop in the voltage profile, change in the state of charge, and the effects of charge and discharge rates during cycling. © 2004 The Electrochemical Society. [DOI: 10.1149/1.1759972] All rights reserved.

Capacity fade in lithium ion batteries has been discussed by numerous authors and analyzed in detail through experiments.[1-3] Although several mathematical models have been published[4,5] which predict the performance of lithium battery during charge-discharge operations, very few models exist which have the capability of predicting the capacity fade of a lithium battery over cycling. Darling and Newman[6] included a side reaction that occurs in a propylene carbonate (PC)/$Li_yMn_2O_4$ system in which they were able to predict the importance of the state of charge and self-discharge of the battery with cycling. Later Arora *et al.*[7] simulated the phenomenon of capacity fade by considering the lithium deposition as a side reaction during over-charge conditions and extended this concept to the increase in the thickness of the surface film with cycling. Recently, Ramadass *et al.*[8] presented an empirical model for capacity fade which includes the state of charge, solid-phase diffusion coefficient, and film resistance as a function of cycle number. Also Ramadass *et al.*[9] presented a semiempirical model for the capacity fade of lithium-ion systems based on the film formation during cycling. In addition, Ploehn *et al.*[10] presented a simple model to predict capacity fade for batteries in storage conditions.

None of these models included the effect of porosity change of the intercalation material on capacity fade which is observed experimentally.[11,12] The plugging of the pores in the electrodes due to side reaction products is also a major cause for the capacity fade of the battery during cycling. The inclusion of the porosity changes due to pore plugging eliminates the need for many empirical relations used in earlier models. The mathematical treatment of the plugging of pores and the subsequent active area changes is similar to the work done by Evans *et al.*[13] on the lithium/thionyl chloride primary cell. The objective of this work is to examine the effect of a side reaction and the porosity changes on the capacity fade of lithium ion batteries.

System Description

The model system considered in this work has a porous $LiCoO_2$ cathode and LiC_6 anode with small amounts of binder and conductive material as shown in Fig. 1. The electrodes are sandwiched using a porous polypropylene separator which is ionically conducting but electronically insulating, filled with 1 M $LiPF_6$ in an ethylene carbonate/dimethyl carbonate (EC/DMC) mixture. The three regions to be modeled are the porous anode, the separator, and the porous cathode. Aluminum and copper foils are used as current collectors for the cathode and anode, respectively. The current distribu-

tions in the current collectors are ignored in the model and so the ends of the cathode and anode are the boundaries of the model and act as current collectors.

The major reactions that occur at the cathode and the anode are the lithium intercalation and deintercalation into the active material, which is based on the following reaction scheme

$$Li^+ + e^- + * \rightleftarrows Li - * \qquad [1]$$

where * is an active site inside the solid insertion material. In attempting to describe the phenomenon of capacity fade, a side reaction which consumes Li^+ is incorporated. A number of reaction mechanisms have been proposed for the electrochemical reduction of solvents on the carbon electrode.[14] The dominant side reaction considered in this model is the formation of lithium diethylene carbonate as a result of the opening up of the structure of ethylene carbonate by a nucleophilic attack. The detailed mechanism of this reaction scheme is discussed by Aurbach *et al.*[15] This reaction is assumed to occur continuously during cycling and as a result some Li^+ ions are lost. The reaction scheme is as follows
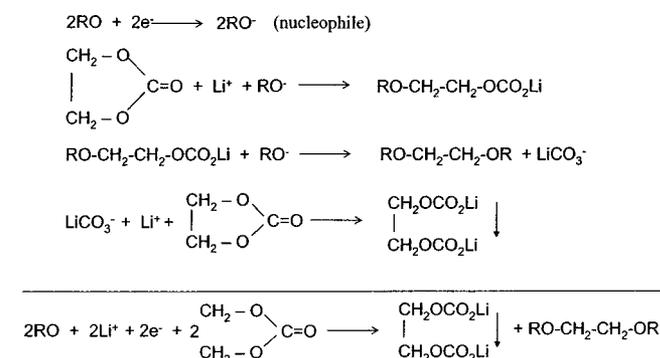
In summary the reaction can be written as

$$2Li^+ + 2CH_2OCOOCH_2 + 2RO + 2e^-$$
$$\rightarrow ROCH_2CH_2OR + (CH_2OCO_2Li)_2\downarrow \qquad [2]$$
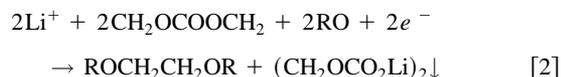
The precipitate formed in Reaction 2 is assumed to be deposited within the pores of the carbon electrode, which in turn decreases the porosity and blocks the active surface area for reaction. To make the model simple the energy transport in the cell is not considered, and volume changes associated with the cell are also ignored.

Model Development

The mathematical model presented here closely follows the model developed by Fuller *et al.*[16] for a dual lithium ion insertion cell which is based on porous electrode theory, as discussed by
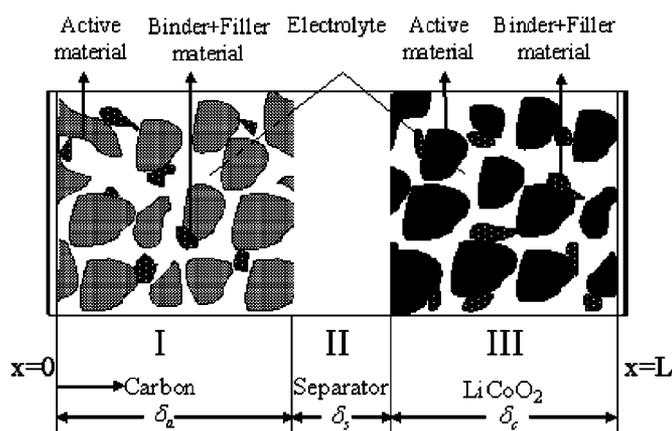
Fig. 1

Figure 1. Schematic of a lithium ion cell consisting of a positive LiCoO$_2$ and negative carbon electrode with a separator.

Newman[17] and by DeVidts and White.[18] The solid matrix and the electrolyte phases are treated as a superposition of two continua. Average values over a unit volume for solution-phase concentrations, pore wall flux, and specific interfacial area were used. Concentrated solution theory is used to treat transport processes in the porous electrodes assuming a binary electrolyte and solvent. For a binary salt and solvent and using the solvent as stationary reference species we can invert the Stefan Maxwell's equations to yield the flux of the species in solution to get[19]

$$\mathbf{N}_+ = -D\nabla c_+ + \frac{\mathbf{i}_2 t_+^o}{z_+ F} \quad [3]$$

$$\mathbf{N}_- = -D\nabla c_- + \frac{\mathbf{i}_2 t_+^o}{z_- F} \quad [4]$$

where c_+ and c_- are the concentrations of the positive and the negative species of the salt and $\mathbf{i}_2$ is the solution-phase current. For a completely dissociated salt the mass conservation yields

$$c = \frac{c_+}{\upsilon_+} = \frac{c_-}{\upsilon_-} \quad [5]$$

Plugging Eq. 5 into 3 the material balance for Li$^+$ in the electrolyte becomes

$$\frac{\partial(\varepsilon_j, c)}{\partial t} = -\nabla\left(-D_{eff}\nabla c + \frac{\mathbf{i}_2 t_+^0}{z^+ \upsilon^+ F}\right) - \sum_{k=1,2} a_j j_{n,j,k}, \quad j = n, p \quad [6]$$

where ε is the volume fraction of the electrolyte phase and $j_{n,j,k}$ is the pore wall flux of the reacting Li$^+$ species in electrolyte phase due to Reaction 1 and 2, ($k = 1,2$), averaged over the interfacial area. Here the porosity is a dependent variable and has to be determined along with the other dependent variables ($c, \phi_1, \phi_2, \mathbf{i}_1, \mathbf{i}_2, j_n$).

The governing equation for the porosity is the overall material balance in the matrix phase

$$\frac{\partial \varepsilon_j}{\partial t} = -\sum_{k=1,2} \sum_i^{\text{solid phases}} a_j j_{s,j,k} \tilde{V}_i, \quad j = n, p \quad [7]$$

where $j_{s,j,k}$ is the pore wall flux averaged over the interfacial area for the individual species in the solid phase and a_j is the surface area to volume ratio which is defined as

$$a_j = 3\left(\frac{1 - \varepsilon_j - \varepsilon_{f,j}}{R_{s,j}}\right), \quad j = n, p \quad [8]$$

where ε_j and $\varepsilon_{f,j}$ are the volume fractions of the electrolyte and the filler materials, respectively, and $R_{s,j}$ is the radius of the spherical particle. Strictly, the inclusion of volume changes due to intercalation should include the change in the radius of the particle with time. This phenomenon is not included here. The quantities $j_{s,j,k}$ and $j_{n,j,k}$ for any species i can be related based on the stoichiometries of Reaction 1 and 2

$$\left.\begin{array}{l} j_{s,j,k} = -j_{n,j,k}, \quad j = n, p, \quad k = 1 \\ j_{s,j,k} = -\frac{1}{2} j_{n,j,k}, \quad j = n, \quad k = 2 \end{array}\right\} \quad [9]$$

where $j_{nj,k}$ is the pore wall flux of the reacting Li$^+$ species in the electrolyte phase.

The variation of the potential in the electrolyte is given as[6]

$$\mathbf{i}_2 = -\kappa_{eff}\left\{\nabla\phi_2 - \frac{2RT}{F}\left(1 + \frac{\partial \ln f}{\partial \ln c}\right)(1 - t_+^o)\nabla \ln c\right\} \quad [10]$$

where ϕ_2 is the solution-phase potential measured with a lithium reference in solution. The above expression is similar to Ohm's law in the solution phase, but it includes the resistance due to concentration variations also. An ideal solution is considered in this case and so $f = 1$.

The current distribution in the solid phase is given by simple Ohm's law

$$\mathbf{i}_{1,j} = -\sigma_{eff,j}\nabla\phi_{1,j}, \quad j = n, p \quad [11]$$

where $\mathbf{i}_{1,j}$ and $\phi_{1,j}$ are the matrix phase currents and potentials, respectively. $\sigma_{eff,j}$ is the effective conductivity. The total current that flows through either the solution phase or the matrix phase is conserved and thus

$$\nabla \cdot (\mathbf{i}_1 + \mathbf{i}_2) = 0 \quad [12]$$

The pore wall flux of the reacting species can be related to the divergence of the current flow in the electrolyte phase using Faraday's law

$$\nabla \cdot \mathbf{i}_{2,j} = -F \sum_{k=1,2} \frac{n}{s_j} a_j j_{n,j,k}, \quad j = n, p \quad [13]$$

The active material is assumed to be made of spherical particles with diffusion being the major mode of transport into the particle. So the mass transport within the particle can be written using Fick's second law for spherical diffusion as

$$\frac{\partial c_{s,j}}{\partial t} = \frac{1}{r^2}\frac{\partial}{\partial r}\left[D_{s,j}r^2\left(\frac{\partial c_{s,j}}{\partial r}\right)\right], \quad j = n, p \quad [14]$$

The intercalation kinetics in either electrode is written in the form of Butler-Volmer expressions with concentration-dependent exchange current density. The expression for such a charge-transfer reaction using Butler-Volmer kinetics becomes

$$j_{nj,k} = k_j(c_L)^{\alpha_{a,j}}(c_{T,j} - c_{s,j})^{\alpha_{a,j}}(c_{s,j})^{\alpha_{r,j}}\left\{\exp\left[\frac{\alpha_{a,j}F}{RT}(\eta_{j,k})\right]\right.$$
$$\left. - \exp\left[\frac{-\alpha_{c,j}F}{RT}(\eta_{j,k})\right]\right\}, \quad j = n, p, \quad k = 1 \quad [15]$$

where k_j is the net reaction rate constant and $\eta_{j,k}$ is the overpotential for the reaction which can be defined as the difference between the solid-phase and the solution-phase potential with respect to the open-circuit potential

$$\eta_{j,k} = \phi_1 - \phi_2 - U_{j,k}, \quad j = n, p, \quad k = 1 \quad [16]$$

It should be noted that the open-circuit potentials $U_{j,k}$ are strong functions of concentrations and the variation of the open-circuit potential with concentration is obtained experimentally through a very slow rate discharge of LiCoO$_2$ and carbon against lithium foil counter and reference electrode in a T-cell.

The rate of the side reaction is assumed to be kinetically controlled. The Tafel rate expression is used to describe the kinetics on the basis that the side reaction is highly irreversible

$$j_{n,j,k} = i_{o,k} \exp\left(\frac{-\alpha_{c,k}\eta_{j,k}F}{RT}\right), \quad j = n, \quad k = 2 \quad [17]$$

Here $i_{o,k}$ is the concentration independent exchange current density and $j_{n,j,k}$ is the pore wall flux of the reacting Li$^+$ species in the electrolyte phase due to Reaction 2. The overpotential, $\eta_{j,k}$ for the side reaction is defined as

$$\eta_{j,k} = \phi_1 - \phi_2 - U_{j,k}, \quad j = n, k = 2 \quad [18]$$

where $U_{j,k}$ is the open-circuit potential of the side reaction. The value of the exchange current density is an adjustable parameter, as experimental details on the kinetics of the side reduction is not available.

As the side reaction proceeds, there is a decrease in the porosity of the negative electrode system because of the clogging of the pores due to the side reaction product and hence the active surface area for intercalation and side reaction decreases as charging continues. This reduction in the available active surface area is given empirically, similar to that of other systems like lithium thionyl chloride wherein lithium chloride precipitates out[13]

$$a_j = a_j^o\left[1 - \left(\frac{\varepsilon_j^o - \varepsilon_j}{\varepsilon_j^o}\right)^{\xi_j}\right], \quad j = n \quad [19]$$

where ξ_j is an empirical factor which can be obtained through experiments, and which represents the morphology of the side reaction product formed. The change in the variable a_j is incorporated in both the intercalation reaction rate and the side reaction rate term as the side reaction products formed block the active sites for further intercalation and side reaction.

Furthermore the solid-phase diffusion coefficient in the porous layer changes due to the plugging of pores and is given by an expression based on the surface coverage.[20]

$$D_{s,j} = D_{s,j}^o\left[1 - \left(\frac{\varepsilon_j^o - \varepsilon_j}{\varepsilon_j^o}\right)^{\xi_j}(1 - \varepsilon_\delta)\right], \quad j = n \quad [20]$$

where the surface coverage is written in terms of porosity using Eq. 19. $D_{s,j}^o$ is the initial solid-phase diffusion coefficient, and ε_δ is the porosity of the deposit.

Boundary and initial conditions.—At the boundaries of the cell, the total current is carried by the solid phase and hence $\mathbf{i}_2 = 0$. Also by equating the flux to be zero at the boundaries we obtain from Eq. 3 or 4 after plugging in Eq. 5

$$\nabla c = 0 \quad \text{at} \quad x = 0, \quad x = L \quad [21]$$

Based on the same reasoning we can get a boundary condition for the solid-phase potential as

$$-\sigma_{\text{eff},j}\nabla\phi_{1,j} = i_{\text{app}} \quad \text{at} \quad x = 0, \quad x = L \quad [22]$$

where i_{app} is the galvanostatic current in the external circuit. The output potential in the cell would be the difference in the solid-phase potentials at $x = 0$ and $x = L$

$$V_{\text{cell}} = \phi_{1,j}|_{x=L} - \phi_{1,j}|_{x=0} \quad [23]$$

Table I. Electrode parameter values.

Parameters	LiC$_6$	LiCoO$_2$
	Electrode parameters	
D_s^0 (m^2/s)	3.89×10^{-14} [a]	1×10^{-13} [a]
σ (S/m)	100[a]	100[a]
c_T (mol/m^3)	30555[e]	51554[e]
ρ (kg/m^3)	5031.67	2291.62
	Thermodynamic and kinetic parameters	
k	4.92×10^{-10} [i]	1.39×10^{-10} [i]
α_c	0.5[a]	0.5[a]
α_a	0.5[a]	0.5[a]
	Design adjustable parameters	
ε^0	0.31[a]	0.39[a]
ε_f	0.1[a]	0.12[a]
R_s (m)	12.5×10^{-6} [a]	8×10^{-6} [a]
ε_s^0	0.59[a]	0.49[a]
brug	1.5[a]	1.5[a]
δ (m)	87×10^{-6} [m]	92×10^{-6} [m]
l (m)	0.462[m]	0.465[m]
b (m)	0.055[m]	0.053[m]

i-evaluated at initial conditions, m-measured from Sony US 18650. 1.5 Ah cells.
[a] Assumed values.
[e] Estimated values.

For the case of the solution potential, since $\mathbf{i}_2 = 0$ at the boundaries of the cell we have from Eq. 21 and 10

$$\nabla\phi_2 = 0 \quad \text{at} \quad x = 0 \quad [24]$$

and since we are interested only in the potential differences the solution-phase potential at the LiCoO$_2$ electrode current collector interface is set to zero

$$\phi_2 = 0 \quad \text{at} \quad x = L \quad [25]$$

At the electrode-separator interface, for all the variables, the fluxes on the left of the interface are equated to the fluxes on the right, except for the solid-phase potentials, because at the electrode-separator interface the total current is carried by the solution phase as a result of which Eq. 11 becomes

$$\nabla\phi_{1,j} = 0 \quad \text{at} \quad x = \delta_a, \quad x = \delta_a + \delta_s \quad [26]$$

For the case of solid-phase diffusion, from symmetry the flux at the center of the particle can be equated to zero. At the surface of the active material, the pore wall flux across the interfacial area is equated to the solid-phase diffusion flux

$$\frac{\partial c_{s,j}(0,t)}{\partial r} = 0, \quad j = n,p \quad [27]$$

$$-D_{s,j}\frac{\partial c_{s,j}(R_s,t)}{\partial r} = a_j j_{n,j}, \quad j = n,p \quad [28]$$

The initial conditions used in the model are

$$\left.\begin{array}{l} c = c^0 \text{ at } t = 0, \ 0 \geqslant x \leqslant L \\ c_{s,j} = c_{s,j}^0, \ j = n,p \text{ at } t = 0, \ 0 \geqslant x \leqslant L \\ \varepsilon_j = \varepsilon_j^0, \ j = n,p \text{ at } t = 0, \ 0 \geqslant x \leqslant L \end{array}\right\} \quad [29]$$

Model parameters and solution method.—The parameter values used in the model are listed in Table I and Table II. The values for the transport properties of the electrolyte, the bulk diffusion coefficient (D_b), transference number (t_+^0) are taken to be constants. The concentration dependence of the electrolyte conductivity for an EC/DMC mixture is given in the Appendix. The polypropylene separator is inert and porous, filled with the electrolyte in the void spaces. The cycling regime of Li$^+$ ions in the cathode and the anode

Table II. Parameter values used for the simulation.

| Parameter	Value
D_b (m²/s)	7.5×10^{-10} [23]
c^0 (mol/m³)	1000[a]
t_+^0	0.373[a]
f	1[a]
V_{Li-*} (m³/mol)	5.607×10^{-6} [e]
V_{LAC} (m³/mol)	64.39×10^{-6} [e]
ξ	0.15[a]
T (K)	298[a]
κ_0 (S/m)	100[a]
a_j^0 (m²/m³)	156000[a]
ε^s	0.723[a]
brug^s	0[a]
Parameters for side reactions	
α_c	0.5[a]
i_0 (A/m²)	1×10^{-5} [a]
U	0.4[a]
ε_δ	0.4[a]

[a] Assumed values
[e] Estimated values.

are $0.53 < \Delta y < 1$ and $0 < \Delta y < 0.9$, respectively, where Δy denotes the degree of intercalation. Data regarding thermodynamics and kinetics of insertion reactions are not readily available as they are hard to measure.[10] The rate constant for the lithium intercalation and deintercalation reaction is evaluated at initial conditions. The transfer coefficients for the lithium intercalation and deintercalation reaction are assumed to be 0.5. The functional dependence of the open-circuit potential on the amount of lithium inserted may widely vary with regard to the chemistry of the system. First principles calculations on the open-circuit potential are available;[21] however in our studies the open-circuit potential of individual electrodes are obtained by running a slow rate discharge (C/30) in a T-cell against a Li/Li⁺ reference and fit empirically to use it in the model (Appendix A). The exchange current density and the transfer coefficient of the side reaction are fitting parameters, as experimental data are not available. The maximum concentrations in the positive and the negative electrode are evaluated from the density and the molecular weight of $LiCoO_2$ and LiC_6, respectively. The open-circuit potential of the side reactions has been studied in detail by various authors,[15,22] and different mechanisms yield a range of equilibrium potentials. However in this model the equilibrium potential is assumed to be 0.4 V *vs.* Li/Li⁺ around which most of the reduction parasitic reactions occurs.

The design-adjustable parameters in the model include electrode thickness, separator thickness, initial porosity of the electrodes, porosity of the separator, and volume fraction of the filler material. In this model these values are measured from a commercial Sony U.S. 18650 cell. The system of the above partial differential equations is solved numerically using FEMLAB which uses the finite element method to discretize the governing equation.

Results and Discussion

The simulation for the initial cell performance during charging is done with the inclusion of the porosity variations due to both the intercalation and the side reaction product formed. However, for the simulation of the capacity fade process, the volume changes due to the intercalation reaction are ignored because they are reversible, but the volume changes due to the irreversible side reaction product formed are considered. A detailed explanation of this assumption is discussed later. The charging rate used for the fresh cell performance analysis and for the cycling simulations are 27.8 A/cm².

Figure 2 shows the simulated charging profile of a fresh lithium-ion battery. In this specific system the positive electrode is the limiting electrode. The charging rate $i_{app} = 27.8$ A/m² chosen to ana-
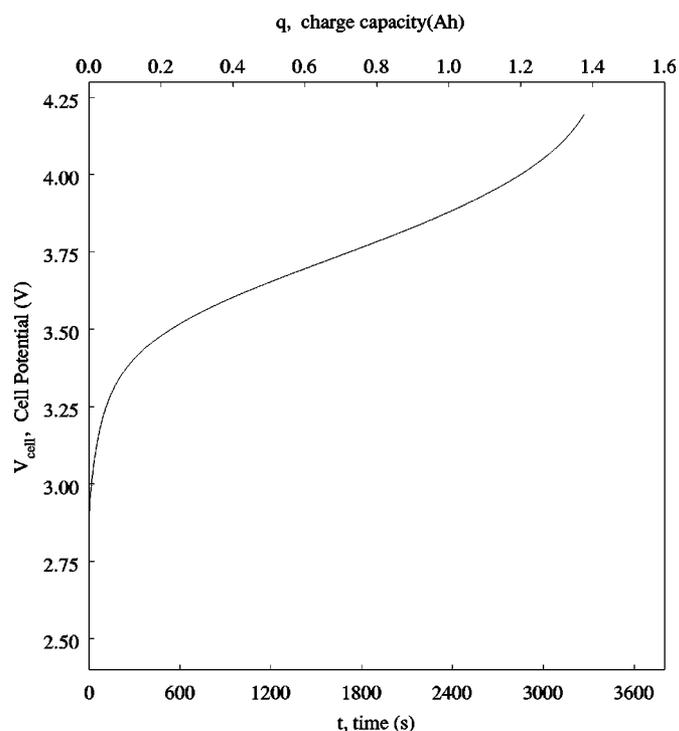
Figure 2. Simulated charging profile of a fresh lithium ion battery at a charging rate of 27.8 A/m² (C rate).

lyze capacity fade was sufficiently low so that it does not entail a constant voltage charging part and almost complete charging is effected through the galvanostatic charging. This is also evident from the charging voltage profile shown from which it can be inferred that almost complete charge capacity is delivered during charging. Since most of the capacity is obtained before reaching the cutoff potential, the intercalation reactions were not diffusion controlled at this rate of charging. The inclusion of a film resistance term (R_f) in the model in Eq. 16 would contribute additional overpotential to the cell to match the experimental charging profiles. However, the film resistance term is neglected in this model since its practical source is not known precisely. But the changes in porosity with cycling introduce additional resistance to the cell which is explained later in detail.

A typical concentration profile for the fresh cell across the electrode, over a time scale with an initial concentration of 1000 mol/m³ ($\bar{c} = 0$) has been depicted in Fig. 3. A distinct concentration profile is established at a short time because of the low value of the dimensionless parameter S_e, where S_e is defined as the ratio of the diffusion time to the charging time

$$S_e = \frac{L^2 i_{app}}{D(\varepsilon_j^o)^{brug} nF(1 - \varepsilon_j - \varepsilon_{f,j})(c_{T,j} - c_{s,j}^o)\delta_c} \quad [30]$$

For the case of galvanostatic charging, with the charging current equal to 27.8 A/m², the calculated value of S_e for $LiCoO_2$ is 0.055. Because of the fact that the time for transport is small when compared to the time for discharge, a steady state is attained for the concentration profile although there is transience in the output voltage profile. Thus an almost fully developed concentration profile or a quasi-steady-state profile is attained even at early stages of charging.

From the concentration profiles it can be inferred that at this rate of charging, electrode thickness, and initial salt concentration, the effect of concentration polarization is not so high as to drive the concentration to zero anywhere within the electrode. As a result the limiting phenomenon of solution-phase diffusion is not reached and complete utilization of the material is not hindered due to concen-
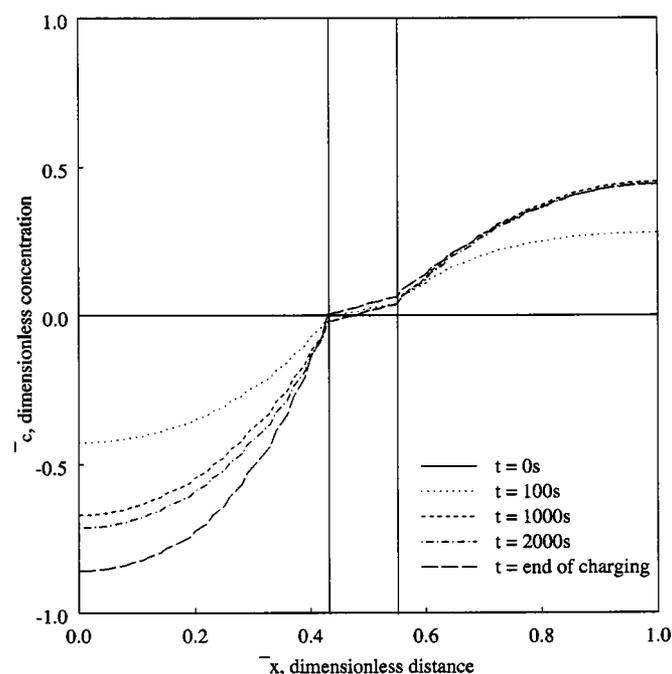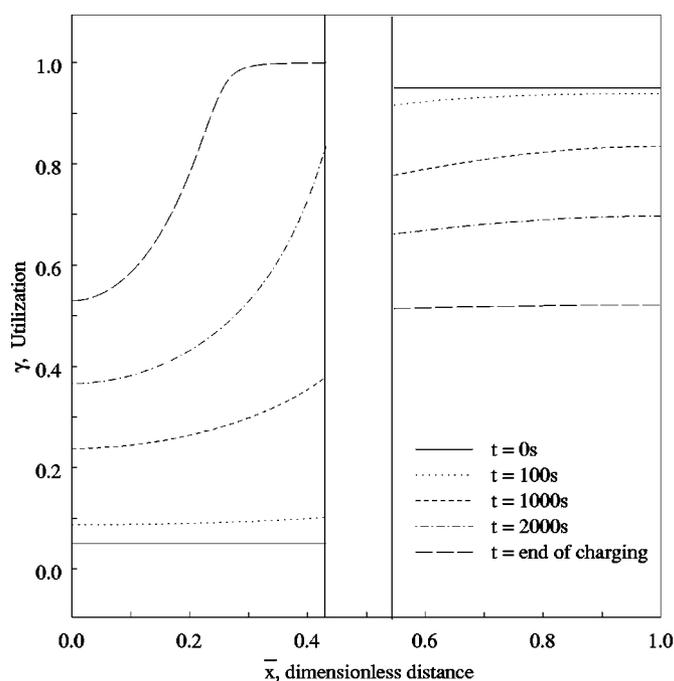
Figure 3. Simulated profiles of the dimensionless local concentration across the full cell during galvanostatic charging of a fresh lithium ion battery at a rate of 27.8 A/m^2 (C rate).

Figure 4. Variation of local utilization across the full cell during the galvanostatic charging of a fresh lithium ion battery at a rate of 27.8 A/m^2 (C rate).

tration gradients within the porous electrode. Moreover the concentration profiles in the negative electrode do not reach the quasi-steady-state form as opposed to the positive electrode, where it reaches the quasi-steady-state form before the end of charging. This suggests that the reaction zone is uniformly distributed in the positive electrode while in the negative electrode the reaction front has sharp profiles. The low value of the porosity in the negative electrode and the continuously decreasing porosity due to the plugging of the pores as a result of the side reaction, in addition to the intercalation reaction, causes steeper concentration gradients in the carbon electrode to yield to the reaction rate.

Figure 4 presents the local utilization, γ [ratio of the average solid-phase concentration ($\bar{c}_s$) the theoretical maximum material concentration (c_T)] of active material across the full cell during the galvanostatic charging of a fresh cell at 1C rate. Within the cycling regime the local utilization across the positive electrode is more or less uniform, while the utilization in the negative electrode has distinct profiles. This is because of the fact that the reaction rate distribution in the positive electrode (see Fig. 5) levels out evenly after a very high reaction rate at the separator electrode interface for a short time. But in the case of the negative electrode the reaction rate distribution is maximum at the separator electrode interface at the start and towards the end of charging, the reaction front moves across the depth of the electrode as the utilization becomes complete in the front portion of the electrode. The detailed explanation of this phenomenon is found in Ref. 16.

The porosity distribution within the full cell during charging for a fresh cell is presented in Fig. 6. The porosity profile within the separator is constant and equal to the initial porosity of the separator and is not presented in the figure. It should be noted that the variation of porosity within the electrode is due to the lithium intercalation reaction and the parasitic side reaction. In the case of the negative electrode the side reaction causes additional changes in the porosity due to the precipitate formed, apart from the porosity change due to the intercalation reaction. The steeper concentration gradient in the negative electrode is an outcome of this effect. However, the side reaction is absent in the case of the positive electrode. Although it was found that the intercalation reaction predominantly

determines the porosity profile, the minor porosity changes due to the side reaction is more crucial in determining the capacity fade of the battery. This is because the porosity changes due to intercalation will be canceled out once the subsequent discharge step is carried out; however the porosity changes due to the side reactions are irreversible as the side reaction product formed permanently plugs the pores of the intercalation material. As it is seen from Fig. 6 the porosity falls off to lower values at the separator electrode interface because both the intercalation-deintercalation reaction rate and the side reaction rate (shown in Fig. 7) are maximum at the electrode
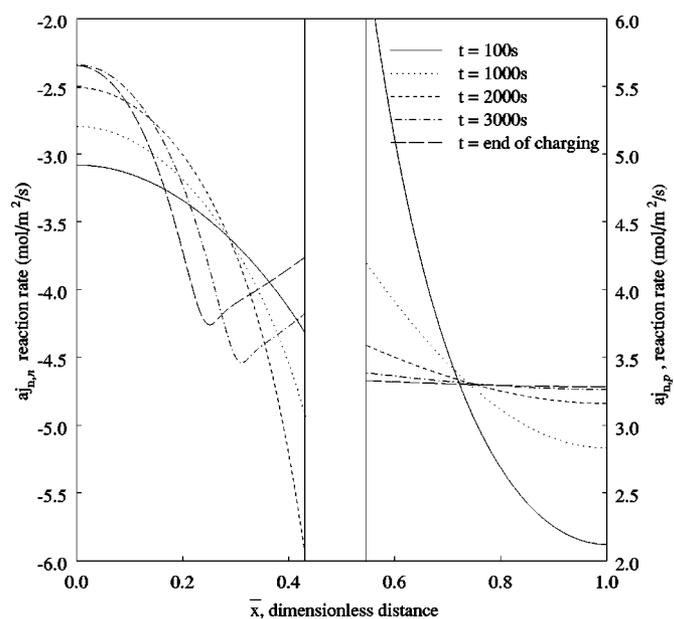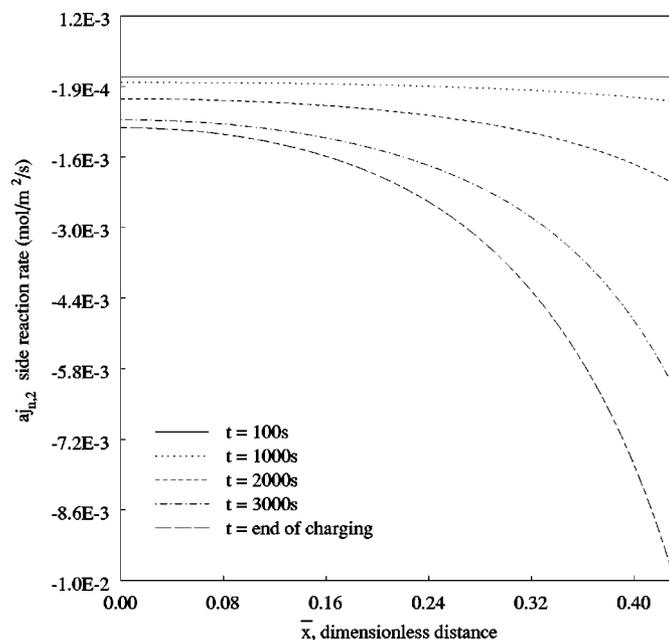

Figure 5. Variation of the intercalation reaction rates across the full cell at various times during galvanostatic charging of a fresh lithium ion battery at a rate of 27.8 A/m^2 (C rate).
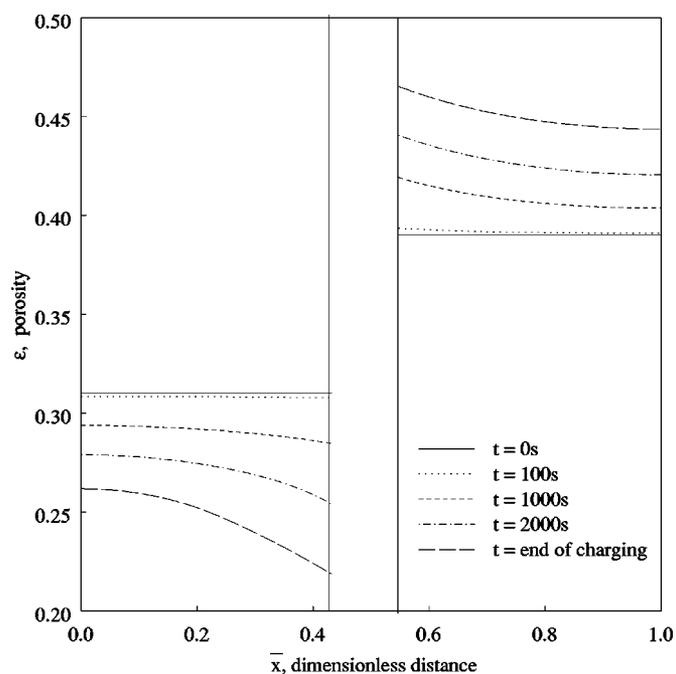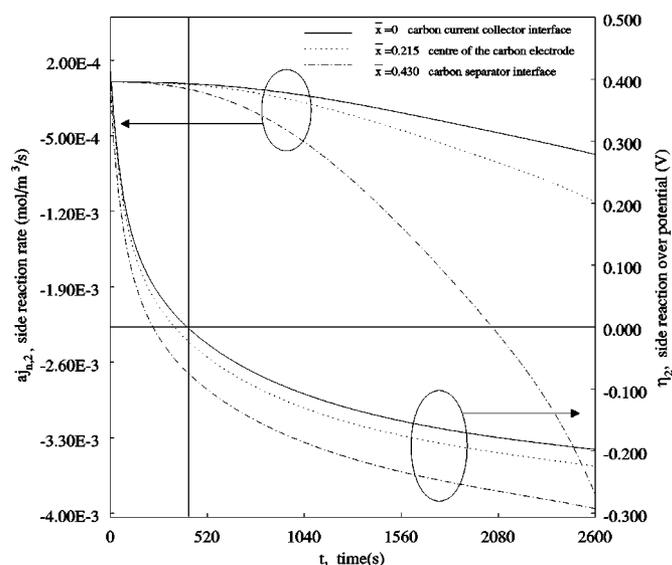
Figure 6. Simulated profiles of the variation in porosity across the full cell at various times during galvanostatic charging of a fresh lithium ion battery at a rate of 27.8 A/m^2 (C rate).

Figure 8. Plot showing the initiation of side reaction at negative overpotentials and the increase in the side reaction rate with time at various points across the carbon electrode. This plot also predicts that the side reaction starts earlier at $\bar{x} = 0.43$ than at $\bar{x} = 0.215$ or $\bar{x} = 0$. Simulated profiles are for the galvanostatic charging of a fresh lithium ion battery at a rate of 27.8 A/m^2 (C rate).

separator interface. The value of the partial molar volume of the species is a key parameter, which determines the extent of the porosity change within the electrode during charging. The value of the partial molar volume of the side reaction product formed and Li$^+$ are 64.39 $\times$ 10^{-6} and 5.607 $\times$ 10^{-6} m^3/mol, respectively.

Figure 8 shows the overpotential of the side reaction with time at various points across the negative electrode for the fresh battery. During the start of charging the overpotential is positive at the ends

and the center of the electrode and since the side reaction is assumed to be a reduction reaction which obeys the Tafels relation, the reaction is not facilitated at positive overpotentials. This can be confirmed by noting that the reaction rate of the side reaction is close to zero at the different regions in the cell during the initial stages of charging. However, as charging proceeds the side reaction overpotential crosses the equilibrium potential and passes over to negative values. Initially this occurs at the carbon electrode separator interface as seen in the figure and later the reaction starts at the back of the electrode also. The side reaction rate then continuously increases with time until the charging is stopped.

Capacity fade analysis.—The above model is extended to analyze the capacity fade of lithium-ion battery. The side reaction involved during charging occurs continuously over cycling. The amount of charge lost to the side reaction is calculated at each cycle using the model and the total amount of available charge for the next cycle is updated based on the loss in the previous cycle. The Faradaic charge lost, due to the side reaction at any cycle number, N, can be evaluated by integrating the local side reaction rate over the carbon electrode
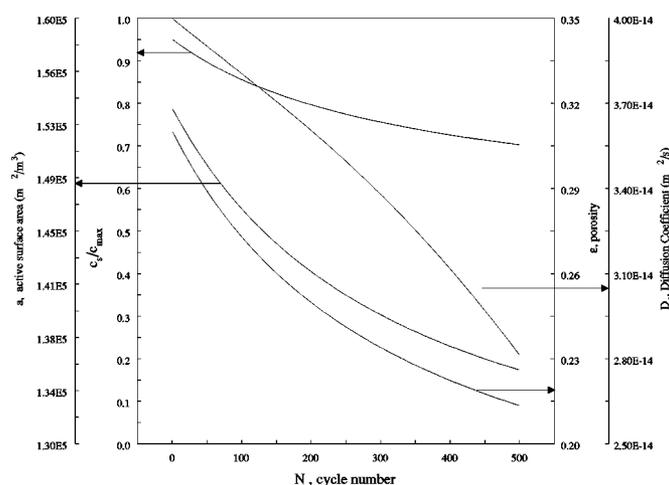
$$q_2|_N = a_j F l b \int_{t=0}^{T} \int_{x=0}^{\delta_a} j_{n,j,k}|_N \, dx \, dt, \quad j = n, k = 2 \quad [31]$$

where the limits of the integration are over the thickness of the carbon electrode (δ_a) for the spatial integration and over the total charging time (T) for the time integral. So the net charge available for the $N + 1$th cycle would be

$$q|_{N+1} = q_1|_N = q|_N - q_2|_N \quad [32]$$

where q_1 and q_2 are charge consumed by the intercalation reaction and side reaction, respectively, and q is the total charge capacity available in any cycle. The total initial theoretical capacity of the cell (just before the cycling starts) is calculated from the relation

$$q|_{N=1} = (1 - \varepsilon_j^o - \varepsilon_{f,j}) l b \delta_c y_j F \theta_j^o c_{T,j}, \quad j = p \quad [33]$$

Figure 7. Simulated profiles of the variation in reaction rate of the side reaction occurring on the negative electrode, at various times during galvanostatic charging of a fresh lithium ion battery at a rate of 27.8 A/m^2 (C rate).

Figure 9. Plot showing the change in the average values of various parameters with cycling. Cycling simulations are done for galvanostatic charging at a rate of 27.8 A/m^2 (C rate).

Figure 10. Variation of porosity across the carbon electrodes at cycle numbers 1, 200, 500 obtained at the end of charging. The porosity changes due to intercalation of Li$^+$ and the side reaction are included. Cycling simulations are done for galvanostatic charging at a rate of 27.8 A/m^2 (C rate).

where Δy is the intercalation coefficient and l, b, δ_c are the dimensions of the electrode. The value of this capacity available for intercalation goes on decreasing depending on the extent of the side reaction rate. Here θ_j^o ($c_{s,j}^0 / c_{T,j}$) is defined as the initial state of charge where $c_{s,j}^0$ is the initial concentration available at the start of the first cycle and $c_{T,j}$ is the maximum concentration in the electrode which is calculated from the density and the molecular mass of the electrode material. Since the positive material is limiting, the theoretical capacity is evaluated based on the positive electrode.

To reduce cumbersome modeling the porosity variations due to lithium intercalation and deintercalation were ignored during simulation of cycling process, and the variation of porosity due to the side reaction alone is considered. This assumption should be reasonable because the changes in porosities due to intercalation cancels out during deintercalation as explained previously. This is also a reasonable assumption while we are interested at the overall capacity fade of the battery. This assumption also allows us to run the simulations only for the charging process and save computational time. Thus we can determine the capacity loss at each cycle, assuming the columbic efficiency (ratio of the charge capacity to the discharge capacity) to be unity within a cycle. The parameters which are averaged over the end of the each cycle for setting up the initial conditions for the next cycle are the active surface area (a_j), porosity (ε_j), and diffusion coefficient ($D_{s,j}$) and are calculated as follows

$$\left\{ a_j^0 \big|_{N+1} = \frac{\int_0^{\delta_a} a_j dx \big|_N}{\delta_a}, \quad D_{s,j}^0 \big|_{N+1} = \frac{\int_0^{\delta_a} D_{s,j} dx \big|_N}{\delta_a}, \right.$$

$$\left. \varepsilon_j^0 \big|_{N+1} = \frac{\int_0^{\delta_a} \varepsilon_j dx \big|_N}{\delta_a} \right\}, \quad j = n \qquad [34]$$

The integrals are evaluated at the end of charging time ($t = T$). The changes in average values of these parameters at the end of charge at each cycle are shown in Fig. 9. The rate of change of average porosity decreases with cycling due to the fact that, as more reaction product is formed, it hinders the side reaction rate because of the decrease in the interfacial area.

Figure 10 depicts the variation in the porosity profile at specific cycle numbers across the carbon electrode. The plots are obtained by running the charge model with the updated values of the porosity, active surface area, diffusion coefficient, and state of charge for the specific cycle numbers (1, 300, and 500) with the variations in porosity due to the intercalation reaction included. All the porosity profiles in Fig. 10 are obtained at the end of charging. It can be seen
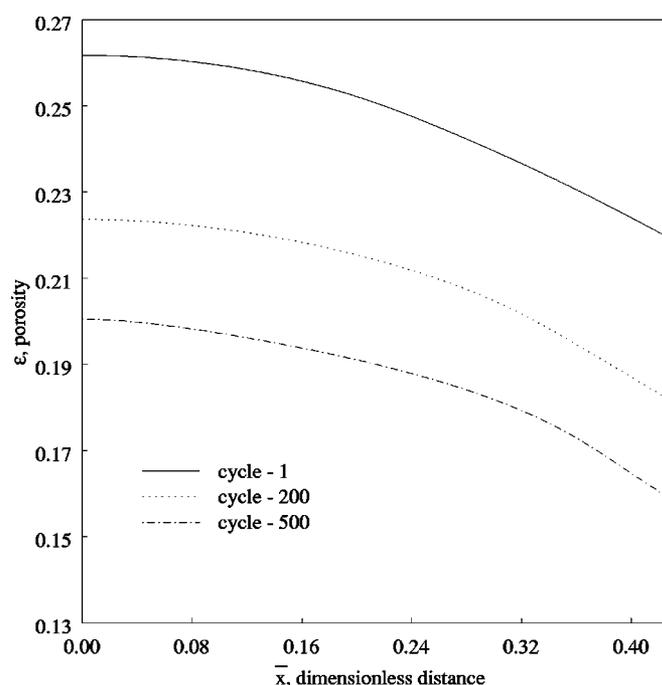
that when the change in the porosity due to the intercalation reaction is also included the porosity profiles falls off to very low values in the carbon electrode toward the end of charging. The subsequent discharge will cancel out the porosity variations due to intercalation and, effectively, changes in porosity observed will be due only to the side reaction.

Effect of porosity, diffusion coefficient, and state of charge.—The effect of the change in porosity, diffusion coefficient, and state of charge with cycling, on the discharge voltage profile are shown in Fig. 11. To analyze the impact of each of these parameters, the voltage profiles were simulated for the following cases: (*i*) constant initial porosity and constant initial diffusion coefficient for all cycle numbers with the reduced state of charge for the respective cycle numbers, (*ii*) constant initial porosity for all cycle numbers and average diffusion coefficient and reduced state of charge at respective cycle numbers, (*iii*) average porosity, average diffusion coefficient, and reduced state of charge at the respective cycle numbers. For the above three cases the simulations were done at the end of 1, 200, and 500 cycles, respectively.

On comparing the discharge curve obtained at cycle 1 and cycle 200 with case (*i*) we can observe that the change in the state of charge by itself brings a shift in the discharge plateau and the decrease in the run time of the battery. However, this downward shift in the voltage profile largely depends on the open-circuit potential. If the open-circuit potential has a distinct profile with the state of charge, this shift in the plateau can be observed. However in cases where the open-circuit potentials are independent of the state of charge for a very wide range, this shift in the voltage profile with cycling will not be obtained. At 200 cycles with case (*ii*) the discharge curve is simulated with the diffusion coefficient and the state of charge corresponding to that particular cycle number with the porosity being held constant (initial porosity). It can be observed that the change in the diffusion coefficient does not bring about a shift in the discharge plateau; however, the obtained discharge capacity slightly decreases due to the decreased rate capability at lower diffusion coefficients. This capacity lost due to the decrease in the diffusion coefficient can
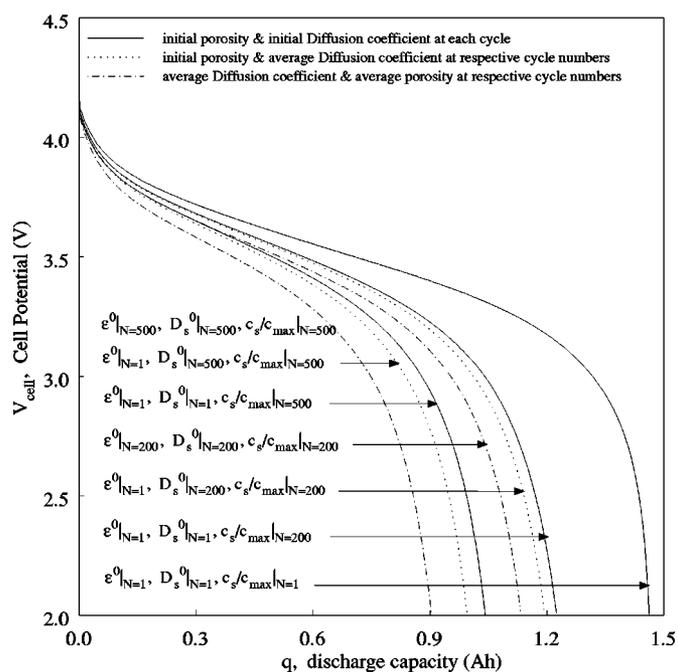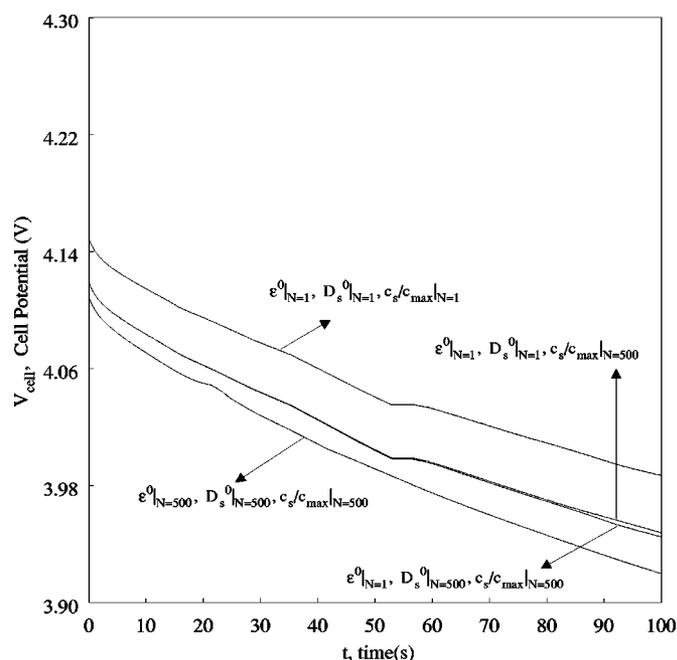
Figure 11. Simulated discharge profile showing the effect of porosity, state of charge, and diffusion coefficient with cycling. The above discharge curves are the simulated profiles at the end of 1, 200, and 500 cycles for various conditions as marked on the plot. The discharge rate used for the simulations is 13.93 A/m^2 (C/2 rate).

Figure 12. Simulated discharge profile for short times showing the effect of porosity and the state of charge in determining the initial Ohmic resistance of the system and the shift in the discharge curve. The change in the diffusion coefficient did not alter the initial resistance and the discharge profile of the cell during the initial part of the discharge.

be recovered at low rates of discharge. For case (*iii*) at 200 cycles, the porosity was also changed to the average porosity obtained at that cycle. In this case it was found that the potential plateau shifted further down, and there was also a decrease in the obtained discharge capacity. This shift in the potential profile is irrespective of the state of charge and is because of the decrease in the porosity which in turn decreases the value of effective solution conductivity and hence the increased ohmic drop. In addition, the decrease in porosity would introduce higher concentration gradients and one can expect higher values of concentration overpotentials with cycling. Both these factors clubbed together with the decrease in the state of charge and diffusion coefficient will determine the shape of the discharge curve at the end of any cycle. These changes are in agreement with experimental data.[1,3] The same explanation holds good for the simulations done at the end of 500 cycles. In fact, the effect of porosity changes are more sensitive to the shape of the discharge curve at higher cycle numbers. The effect of porosity, state of charge, and diffusion coefficient on the discharge curve can be seen more clearly in Fig. 12, which was obtained for short times. The increased ohmic drop with the change in porosity and the impact of the diffusion coefficient, which does not alter the discharge profile at short times, but closes down on the *x* axis at later times, can be clearly observed.

The decrease in the porosity with cycling causes a serious limitation to the utilization of the active material at high cycle numbers even at moderate rates of charging. This is because of the steeper concentration gradients at higher cycle numbers. Figure 13 shows the concentration profiles across the full cell at the end of charging at 1, 200, and 500 cycles. An increased concentration gradient at the start of charging in the negative electrode over that of the positive electrode aggravates and drives the concentration at the back of the negative electrode to zero ($\bar{c} = -1$) at the end of 500 cycles.

Effect of discharge rate.—Figure 14 shows the effect of the discharge rate on the discharge capacity of a fresh battery, *i.e.*, the rate capability of the system. At very high rates the battery could not be theoretically discharged to 2.0 V because of the fact that the salt

concentration drops to zero due to high reaction rates. Also at higher rates the concentration overpotentials are higher and the limiting potential is reached before complete utilization has occurred. This effect of the discharge rate was observed in cycled cells also. We tried to capture this phenomenon of rate capability using the present model and its effect over cycling. It was found that the rate capabil-
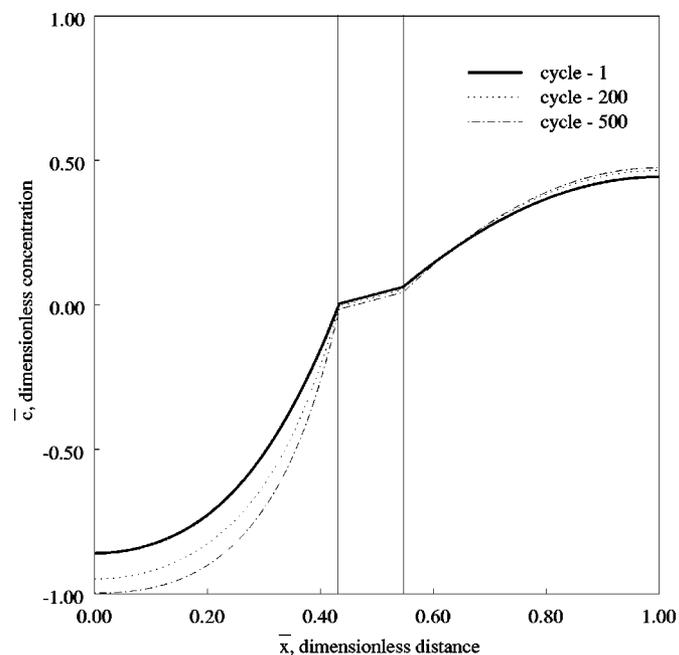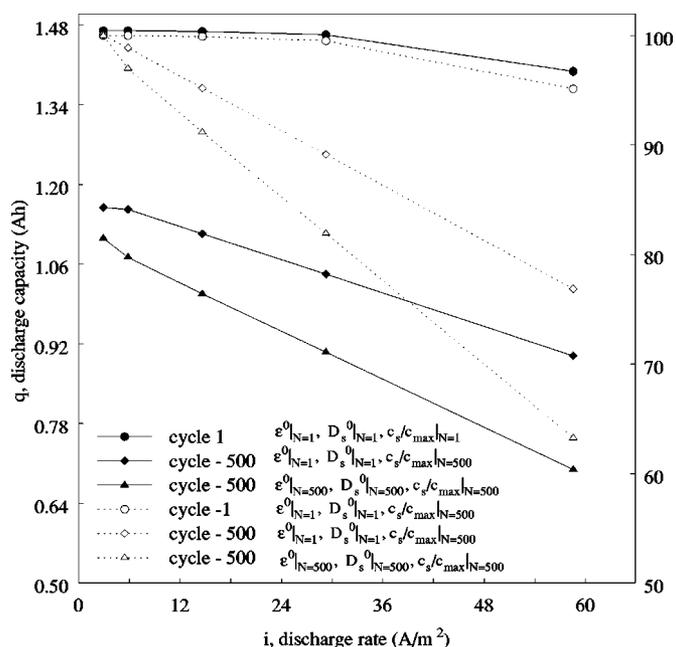

Figure 13. Simulated concentration profiles across the electrode at various cycle numbers (1, 200, 500). All the profiles are obtained at the end of charging at the respective cycle numbers. Cycling simulations are done for galvanostatic charging at a rate of 27.8 A/m^2 (C rate).
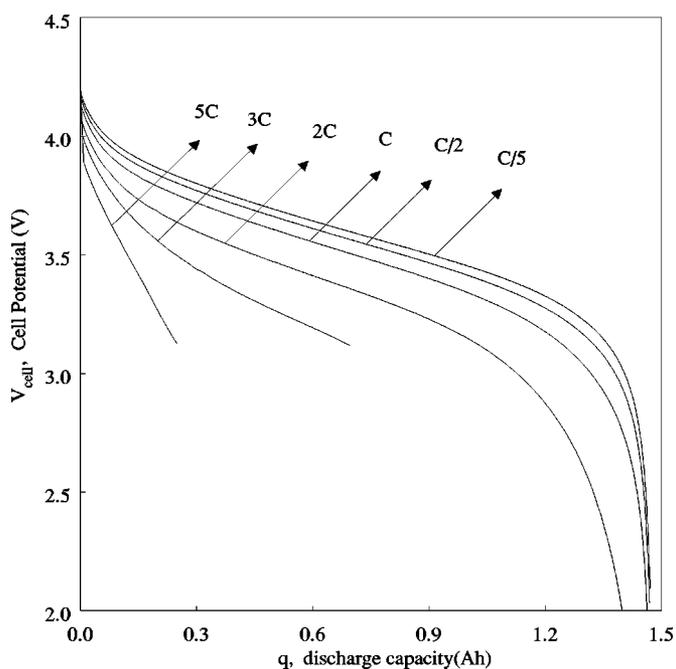
Figure 14. Effect of discharge current density on the discharge capacity of the battery. The solid lines represent the discharge curves at current densities of 5.57 A/m^2 (C/5), 13.93 A/m^2 (C/2), 27.87 A/m^2 (C), 55.75 A/m^2 (2C), 83.63 A/m^2 (3C), and 139.35 A/m^2 (5C), as indicated by the markers.
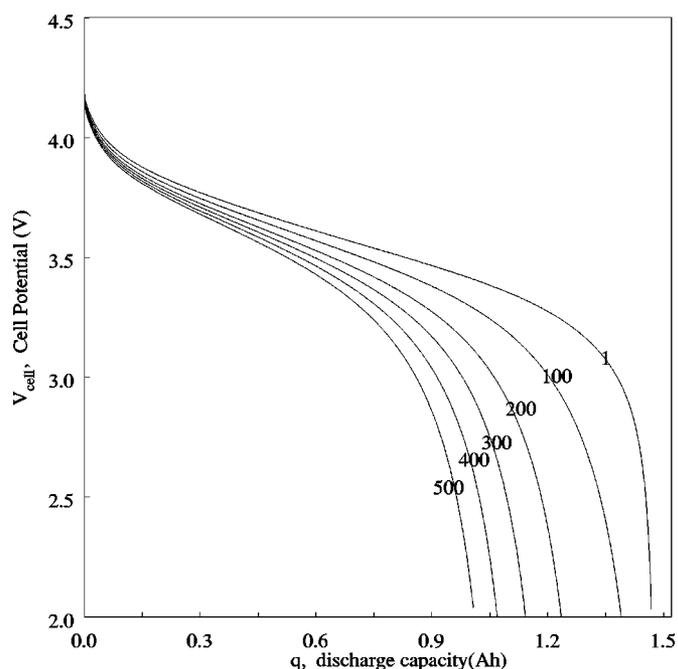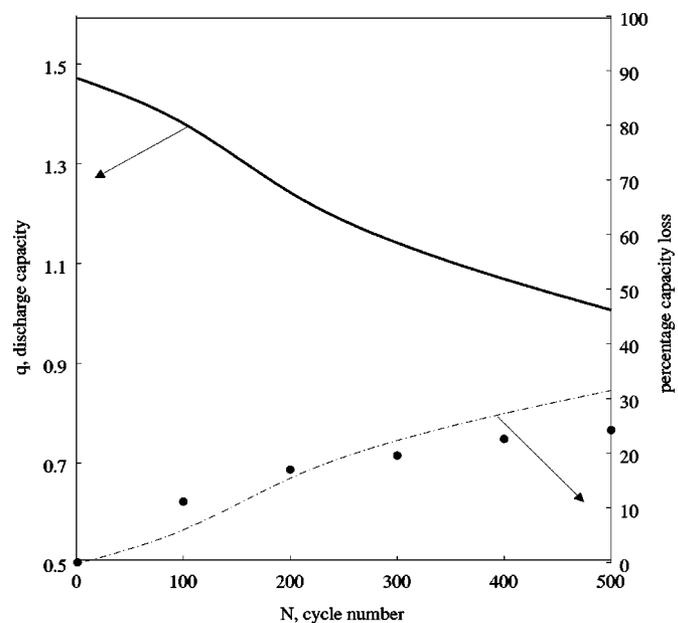

Figure 16. Simulated discharge profiles depicting the capacity fade at cycle numbers as marked on the curves. The discharge rate used for the simulations is 13.93 A/m^2 (C/2 rate).

ity decreased with cycling. While there was a 7.9% decrease in discharge capacity on discharging a fresh cell at 2C rate over that of C/5 rate, the value increased to around 49% after 500 cycles of charging at the C rate with the inclusion of porosity changes. The extent of rate capability was even worse at higher rates of discharge. Figure 15 shows the effect of rate capability with cycling for the case of discharge for a fresh cell, for a cell cycled for 500 cycles

Figure 15. Effect of discharge current on the discharge capacity of the battery (rate capability). The graph above is plotted with the simulated values for a fresh cell and for the cell cycled for 500 cycles (with and without porosity and diffusion coefficient variations with cycling). The plots with dotted lines correspond to the axes on the right (discharge rate *vs.* percentage discharge capacity obtained) clearly show the decreased rate capability with cycling. The effect of porosity changes on rate capability with cycling is observed at high rates of discharge. The lowest discharge rate used for the studies corresponds to the C/10 rate, and the discharge capacity obtained at this rate is assumed to be 100% in this plot.

Figure 17. Simulated values of discharge capacity in the cell as a function of cycle number. The plot (dotted line) corresponding to the axes on the right shows the simulated percentage capacity fade with cycling. The markers are the experimentally obtained values for percentage capacity fade from Sony U.S. 18650 cells. The discharge rate used for the simulations is 13.93 A/m^2 (C/2 rate).

with only the changes in state of charge considered, and for the case of a cell cycled for 500 cycles where the changes due to porosity, diffusion coefficient, and state of charge are included. The discharge capacity obtained at C/10 rate was taken to be 100% (axis on the right in Fig. 15) and the decrease in rate capability with cycling is clearly seen. It was also evident that the changes in porosity affected the rate capability at higher rates of discharge, although at lower rates a significant change in discharge capacity was not observed over the case in which the porosity changes were not included (see Fig. 15). The decrease in the discharge capacity obtained at C/5 rate and 2C rate after 500 cycles for the case in which porosity changes are not included is much less (~19%) when compared to the case in which the porosity changes are included (~49%). There was also a slight change in the value of the discharge capacity obtained for the case in which the variations due to porosities are considered as compared to constant porosity conditions, even at lower rates. This difference suggests that at higher cycle numbers, the discharge has to be done at much lower rates (<C/20) to extract the completely available capacity.

Figure 16 shows the discharge curves obtained at 1, 200, and 500 cycles. For cycling, simulations were done at C rate of charging and the discharge curves obtained for specific cycles are for C/2 rate of discharge. The loss of capacity is attributed to the change in the state of charge and the porosity variations in the electrode which causes the discharge curve to close down on the axis at shorter run times with cycling. The decrease in porosity with cycling causes an increased ohmic resistance due to the decrease in the effective conductivity and also causes an increased concentration polarization with cycling due to the decrease in the value of the effective solid-phase diffusion coefficient of carbon electrode. From the simulation results the capacity fade of the system was about 29% at the C rate of charging after 500 cycles. Figure 17 shows the capacity fade as a function of cycle number. The discharge capacity obtained was at C/2 rate of discharge. The trend in capacity fade observed by simulations for this particular cell shows an initial slow decrease in the capacity and then a rapid decrease in capacity, which then slows down again. The initial slow decrease is because the design for this cell is such that the positive electrode is limited and hence a slight amount of extra capacity is available on the negative electrode. This causes the discharge capacity to drop down slowly initially until a balance on the cell is established. At higher cycle numbers the side reaction rate slows down due to the fact that the area available for the side reaction decreases considerably and hence the decrease in the rate of capacity fade at higher cycle numbers. This is in close agreement with the experimental values obtained from the cycling studies of Sony US 18650 cells. The disagreement between the values may be due to adjustable parameters used for the side reaction in the model, such as the exchange current density and transfer coefficient of the side reaction. These parameters contribute to the extent of the side reaction which occurs during the charging of the battery and hence the capacity fade. Also the inclusion of the constant voltage part of charging will yield more accurate capacity fade predictions.

Conclusions

A general method for the capacity fade prediction of lithium ion battery system was developed. The model captures the loss of capacity by the inclusion of the side reaction which occurs continu-

ously over cycling. The variation in porosity because of the side reaction product formed with cycling causes the discharge voltage plateau to drop down with cycling. The change in the diffusion coefficient and the porosity of the carbon electrode causes steeper concentration gradients with cycling and hence increased polarization losses at higher cycle numbers. Numerous case studies can be done to observe the effect of parameters such as the end of charge voltage, charging rate, depth of discharge over the capacity fade of battery, without relying on empirical relations.

The variation of surface area and diffusion coefficient on the carbon electrode with the change in the porosity are the only expressions used in the model. Experimental measurements can be done to get a good empirical relation between the variations of active surface area and solid-phase diffusion coefficient as a function of cycle number. The inclusion of the constant voltage part of charging in the model would facilitate the prediction of capacity fade for high rates of charging more accurately. Finally by including the energy equations involved, the effect of temperature over capacity fade can be predicted.

Appendix

Transport Properties of the Electrolyte

The effective diffusion coefficient of Li^+ in $LiPF_6$ is given by the Bruggmens relation

$$D_{eff} = D_b \varepsilon_j^{brug_j}, \quad j = n,p \qquad [A\text{-}1]$$

Similarly the effective conductives of Li^+ in the solid phase and the solution phase are also related by the Bruggmens relationship

$$\sigma_{eff,j} = \sigma_{b,j}(1 - \varepsilon_j - \varepsilon_{f,j})^{brug_j}, \quad j = n,p \qquad [A\text{-}2]$$

$$\kappa_{eff} = \kappa_b \varepsilon_j^{brug_j} \qquad [A\text{-}3]$$

The concentration dependence of the bulk electrolyte conductivity for an electrolyte mixture of 1 M $LiPF_6$ in a 1:2 v/v mixture of EC/DMC at 25°C was fit from experimental data by Doyle and Newman[5] to the following expression

$$\kappa_b = \{1.0793 \times 10^{-4} + 6.7461 \times 10^{-3}c - 5.2245 \times 10^{-3}c^2 + 1.3605 \times 10^{-3}c^3$$
$$- 1.1724 \times 10^{-4}c^4\} \qquad [A\text{-}4]$$

Electrode Thermodynamic Data

The open-circuit potential of the positive electrode ($LiCoO_2$) was fit to the function

$$U = \left\{ \frac{4.707 - 36.129\left(\frac{c_s}{c_T}\right) + 104.813\left(\frac{c_s}{c_T}\right)^2 + 149.491\left(\frac{c_s}{c_T}\right)^3 + 111.818\left(\frac{c_s}{c_T}\right)^4 - 35.705\left(\frac{c_s}{c_T}\right)^5}{1 - 7.598\left(\frac{c_s}{c_T}\right) + 21.779\left(\frac{c_s}{c_T}\right)^2 - 30.959\left(\frac{c_s}{c_T}\right)^3 + 23.632\left(\frac{c_s}{c_T}\right)^4 + 7.8474\left(\frac{c_s}{c_T}\right)^5} \right\} \qquad [A\text{-}5]$$

whereas for the negative electrode the experimental data was fit to the function

$$U = \left\{ \frac{1.997 + 2.472\left(\frac{c_s}{c_T}\right)}{1 + 31.823\left(\frac{c_s}{c_T}\right)} \right\} \qquad [A\text{-}6]$$

Here the ratio of the solid-phase concentration to the total concentration (concentration during which the intercalation coefficient is 1) depends on the amount of lithium inserted in either electrodes. The values of the intercalation coefficient obtained experimentally through a slow rate discharge were 0.53 for $LiCoO_2$ and 0.9 for the carbon electrode.

List of Symbols

a specific surface area of the porous material, m^2/m^3
b height of the electrode, m
brug   Brugmans exponential factor
c solution phase concentration, mol/m^3
$\bar{c}$ dimensionless solution-phase concentration, $(c-c^0)/c^0$
c_s solid-phase concentration, mol/m^3
$\bar{c}_s$ average solid-phase concentration, mol/m^3
c_T concentration in intercalation material for $\Delta y = 1$, mol/m^3
D diffusion coefficient of Li^+ in the salt, m^2/s
D_s diffusion coefficient of Li^+ in the solid phase, m^2/s
f activity coefficient of salt
F Faradays constant, 96,487 C/equiv
i_0 exchange current density, A/m^2
i_1 solid-phase current, A/m^2
i_2 solution-phase current, A/m^2
i_{app} applied galvanostatic current, A/m^2
j_n reaction rate of a species in solution phase, $mol/m^2/s$
j_s reaction rate of a species in solid phase, $mol/m^2/s$
k intercalation reaction rate constant
l electrode length, m
L thickness of the cell, m
M molecular mass, g/mol
N cycle number
n number of electrons
q charge capacity, A h
r radial distance within an active material particle, m
R ideal gas constant, 8.3143 J/mol/K
R_s radius of solid spherical particles, m
S_+ stoichiometric coefficient
t time, s
t^+ transference number
T temperature, K
U open-circuit potential, V
$\tilde{V}$ partial molar volume, m^3/mol
$\bar{x}$ dimensionless distance (x/L)
z charge number

Greek

γ local utilization of the active material in the electrodes $\gamma = (\bar{c}_s/c_T)$
$\delta_a, \delta_c, \delta_s$ thickness of anode, cathode, separator, respectively, m
Δy intercalation coefficient
ε porosity or composite electrode
ε_δ porosity of the deposit
η electrochemical reaction over potential, V
θ state of charge
κ solution phase conductivity, S/m
ξ morphology factor
ρ density of the electrode material, kg/m^3
σ solid-phase conductivity, S/m
ν number of cations or anions into which a mole of electrolyte dissociates
ϕ_1 solid-phase potential, V
ϕ_2 solution-phase potential, V

Subscripts

$-$ negative
$+$ positive
b   bulk values
eff   effective values
i   species
f   filler material
j   positive(p), negative(n) electrode
k   reaction number, [1] intercalation; [2] side reaction
L   electrolyte
s   solid phase
T   concentration in intercalation material for $\Delta y = 1$

Superscripts

0   initial condition
s   separator

References

1. R. Premanand, A. Durairajan, B. Haran, R. White, and B. Popov, *J. Electrochem. Soc.,* **149**, A54 (2002).
2. D. Zhang, B. S. Haran, A. Durairajan, R. E. White, Y. Podrazhansky, and B. N. Popov, *J. Power Sources,* **91**, 122 (2000).
3. G. Sikha, P. Ramadass, B. Haran, R. E. White, and B. N. Popov, *J. Power Sources,* **122**, 67 (2003).
4. M. Doyle, T. F. Fuller, and J. Newman, *J. Electrochem. Soc.,* **140**, 1526 (1993).
5. M. Doyle, J. Newman, A. S. Gozdz, C. N. Schmutz, and J. M. Tarascon, *J. Electrochem. Soc.,* **143**, 1890 (1996).
6. R. Darling and J. Newman, *J. Electrochem. Soc.,* **145**, 990 (1998).
7. P. Arora, M. Doyle, and R. E. White, *J. Electrochem. Soc.,* **146**, 3543 (1999).
8. P. Ramadass, B. Haran, R. E. White, and B. N. Popov, *J. Power Sources,* **123**, 230 (2003).
9. P. Ramadass, B. Haran, P. M. Gomadam, R. White, and B. N. Popov, *J. Electrochem. Soc.,* **151**, A196 (2004).
10. H. J. Ploehn, P. Ramadass, and R. E. White, *J. Electrochem. Soc.,* **151**, A456 (2004).
11. J. Yang, Y. Takeda, Q. Li, N. Imanishi, and O. Yamamoto, *J. Power Sources,* **90**, 64 (2000).
12. L. Y. Beaulieu, K. W. Eberman, R. L. Turner, L. J. Krause, and J. R. Dahn, *Electrochem. Solid-State Lett.,* **4**, A137 (2001).
13. T. I. Evans, T. V. Nguyen, and R. E. White, *J. Electrochem. Soc.,* **136**, 328 (1989).
14. P. Arora, R. E. White, and M. Doyle, *J. Electrochem. Soc.,* **145**, 3647 (1998).
15. D. Aurbach, M. D. Levi, E. Levi, and A. Schechter, *J. Phys. Chem. B,* **101**, 2195 (1997).
16. T. F. Fuller, M. Doyle, and J. Newman, *J. Electrochem. Soc.,* **141**, 1 (1994).
17. J. Newman and C. W. Tobias, *J. Electrochem. Soc.,* **109**, 1183 (1962).
18. H. W. De Vidts and R. E. White, *J. Electrochem. Soc.,* **144**, 1343 (1997).
19. J. S. Newman, *Electrochemical Systems*, p. 268, Englewood Cliffs, NJ (1991).
20. J.-F. Yan, T. V. Nguyen, and R. E. White, *J. Electrochem. Soc.,* **140**, 733 (1993).
21. M. D. Levi and D. Arubach, *Electrochim. Acta,* **45**, 167 (1999).
22. Y. Wang, S. Nakamura, M. Ude, and P. B. Balbuena, *J. Am. Chem. Soc.,* **123**, 11708 (2001).
23. C. J. Ben, B. A. Boukamp, and R. A. Huggins, *J. Electrochem. Soc.,* **126**, 2258 (1979).